Materials Advances

ROYAL SOCIETY OF CHEMISTRY

PAPER

View Article Online
View Journal | View Issue

Cite this: *Mater. Adv.*, 2025, **6**, 5064

Trifunctional $GdCoO_3$ perovskite electrocatalysts for zinc–air battery and water electrolysis applications†

Annet Anna Thomas,‡[a] Anook Nazer Eledath,‡[b] M. Junaid Bushiri[a] and Azhagumuthu Muthukrishnan *[b]

Oxygen electrocatalysts are fascinating due to the absolute necessity of replacing expensive precious metal catalysts in electrochemical energy storage and conversion systems. The $GdCoO_3$ perovskite on N-doped carbon is synthesised using mechanochemical ball-milling followed by pyrolysis. The $GdCoO_3$ on the N-doped carbon composite exhibits better ORR and OER activity with a minimum ΔE value of 0.74 V compared to many other Gd-based perovskites reported in the literature. This material shows promising mass activities estimated from kinetic current densities for the ORR and OER as 18.4 and 19.4 A g^{-1}, respectively. Besides, the materials show HER activity with an overpotential of 0.241 V and a mass activity of 27.7 A g^{-1}. The zinc–air battery performance was demonstrated with a power density comparable to benchmark catalysts. This study features the potential application of the Gd-based perovskites in the field of electrocatalysis.

Received 3rd March 2025,
Accepted 10th June 2025

DOI: 10.1039/d5ma00193e

rsc.li/materials-advances

Introduction

Oxygen reduction and evolution reactions (ORR and OER) are widely known in electrochemical energy storage and conversion. The OER and ORR are commonly employed in metal–air batteries, fuel cells, and water electrolyzers. However, this reversible reaction is kinetically sluggish due to the multi-electron and proton transfer reactions. The reaction rate can be increased using catalysts, typically known as oxygen electrocatalysts. While state-of-the-art metal catalysts demonstrate exceptional performance in the OER and ORR, their cost and scarcity have spurred the development of innovative and more efficient alternatives. The non-noble metal-based earth-abundant metals, mainly transition metal oxides,[1–4] sulfides,[5,6] nitrides,[7,8] and carbides,[9,10] have emerged as cost-effective electrocatalysts for the ORR, OER, and HER.

In search of the various metal oxides for the oxygen electrocatalysts, the perovskite-based bimetallic oxides play a crucial role due to the tunable structural, electronic, and chemical properties, multiple oxidation states, and oxygen vacancies.[11–14] Numerous strategies have been adopted to improve the performance of perovskites, namely partial A-site and/or B-site substitutions, oxygen vacancies, surface and morphology engineering, composites with functionalized carbon, *etc.*[15–17] The semiconducting nature of perovskites necessitates a carbon support to improve their conductivity. Furthermore, the incorporation of N or B heteroatoms into the carbon matrix can further enhance the charge transfer and oxygen adsorption ability.

Lanthanides-based perovskites are known for their strong metal–oxygen bond covalency, rich redox chemistry, and ability to host multiple oxidation states at the B-site and tunable e_g orbital filling improves the intrinsic catalytic activity, enabling enhanced OER/ORR performance.[18–21] Also, La-based perovskites generally show higher thermal and structural stability and better tolerance to harsh electrochemical environments. However, they often exhibit lower electrical conductivity, which can be mitigated through strategies like carbon hybridisation, defect engineering and heteroatom doping.[22,23] Partial substitutions in the A and B sites of La-based perovskites are known for their bifunctional activity towards zinc–air battery applications. The synthesis strategies of the perovskite materials as bifunctional electrocatalysts in zinc–air battery applications are discussed in recent review articles.[19,21] Suntivich *et al.* invented $Ba_{0.5}Sr_{0.5}Co_{0.8}Fe_{0.2}O_{3-\delta}$ (BSCF) for ORR and OER bifunctional activity,[24–26] which was originally developed for solid-oxide fuel cell electrodes.[27] Later, La-doped BSCF was reported for its bifunctional activity comparable to the benchmark catalysts.[28] Other than La, many other elements in the Ln-series are

[a] *Department of Physics, Cochin University of Science and Technology, Kochi 682022, Kerala, India*
[b] *School of Chemistry, Indian Institute of Science Education and Research Thiruvananthapuram, Maruthamala (P.O.), Vithura 695551, Kerala, India. E-mail: muthukrishnan@iisertvm.ac.in*

† Electronic supplementary information (ESI) available. See DOI: https://doi.org/10.1039/d5ma00193e

‡ Equal contribution.

reported for their OER activity. A series of $Ln_{0.5}Ba_{0.5}CoO_{3-\delta}$ (Ln – Pr, Sm, Gd, Ho) were reported for their best activity towards the OER.[25]

Despite a few reports on the other Ln-based perovskites known in the literature, no detailed exploration of their activity has been studied. A recent study reported that sphere-like nanostructured $GdFeO_3$ decorated with PtO_x and NiO nanoparticles is a bifunctional catalyst for the ORR and OER.[29] The $GdMnO_3$ exhibits an onset potential of 0.89 V for the ORR, which proceeds by a $4e^-$ pathway.[30] Recently, Zainab *et al.* synthesised $GdCoO_3$ anchored on nanosheets of g-C_3N_4, exhibiting good electrochemical properties for the OER and HER.[31] The studies by Nandhakumar *et al.* have demonstrated that the nanorod-like morphology of $GdCoO_3$ exhibits an overpotential of 320 mV for the OER.[32] Also, a B-site substitution of $GdFeO_3$ with Cu perovskite-based oxides showed an overpotential of 367 mV, probably due to the higher active surface area.[33]

Herein, we report bimetallic $GdCoO_3$ on N-doped Ketjen Black EC 300 J (KB) carbon towards the ORR, OER, and HER as a trifunctional electrocatalyst synthesised *via* a high-energy ball milling technique followed by pyrolysis in a N_2 atmosphere. To the best of our knowledge, the trifunctionality of the $GdCoO_3$/NC composite has been studied for the first time. Significantly, the $GdCoO_3$/NC composite exhibits a lower η_{10} overpotential of 330 mV for the OER and 241 mV for the HER and an onset potential and half wave potential of 0.93 and 0.82 V *vs.* RHE for the ORR in alkaline medium. Thus, a low bifunctionality index of 0.74 V is achieved, which is lower than many perovskite-based oxides reported in the literature. A liquid electrolyte rechargeable zinc–air battery (RZAB) was demonstrated using the perovskite-based catalyst.

Experimental section

Synthesis of $GdCoO_3$ and the $GdCoO_3$/NC composite

The $GdCoO_3$ (GCO) catalyst was synthesised using the previously reported molten salt synthesis.[34] Briefly, 2.5 mmol of nitrate salts of gadolinium and cobalt and 5 mmol of citric acid were taken in an alumina boat. Then, a trace amount of deionised water was added, and the resulting mixture was calcined using a furnace in an air atmosphere. The calcination was done at 800 °C with a ramp rate of 5 °C min^{-1} for 3 hours. The synthesis procedure of Gd_2O_3 (GdO) and Co_3O_4 (CoO) was similar to that of $GdCoO_3$ by adding the corresponding metal nitrates, thus obtaining individual oxides of Gd and Co.

The $GdCoO_3$/NC composite was synthesised *via* a high-energy wet ball milling technique followed by a heat treatment in N_2 atmosphere. For the wet ball milling process, the synthesised GCO, acid-washed KB, and urea were taken in a stainless-steel (SS) jar in a 1 : 2 : 4 weight ratio and ethanol was added to make a slurry. The 3 mm diameter SS balls were added to the mixture and milled at 500 rpm for about 12 hours in a high-energy ball miller (Retsch PM 100). The resulting sample was then subjected to a heat treatment at 400 °C in an N_2 atmosphere for two hours at a ramp rate of 5 °C min^{-1}. The sample

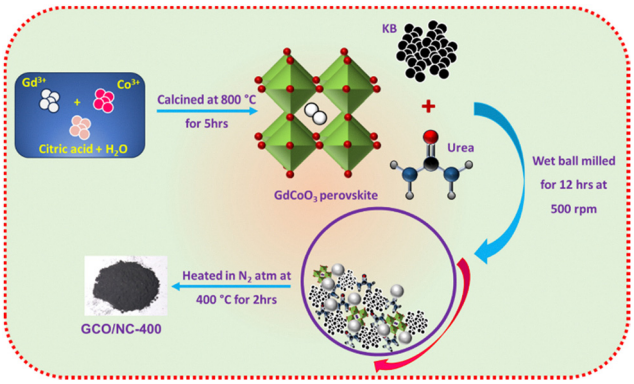

Fig. 1 Schematic representation of the synthesis of $GdCoO_3$-N-doped carbon composites and the control samples.

is denoted as GCO/NC-400. The temperature was optimised to 400 °C due to the decomposing nature of $GdCoO_3$ with carbon and nitrogen precursors at higher temperatures (Fig. S1, ESI†).[35] A schematic representation of the synthesis protocol is shown in Fig. 1. The nitrogen-doped KB composites with GdO/NC-400 and CoO/NC-400 were also prepared as controlled samples using a similar methodology. Also, GCO/C-400 was synthesised without nitrogen precursor. The temperature, time, and ramp rate were optimised. The weight ratio of GCO : KB : urea content was also optimised to obtain the best electrocatalyst for ORR, OER, and HER applications. Table S1 (ESI†) gives a detailed description of the control samples.

Material characterisations

The synthesised materials were characterised using various spectroscopic and microscopic techniques. The phase purity of all the samples was confirmed using the X-ray diffraction pattern (Bruker XRD, Cu Kα, λ = 1.5406 Å, 40 kV, 40 mA). Raman measurements were done using an HR800 LabRAM confocal Raman spectrometer. The morphological characterisations were done using a field emission scanning electron microscope (FE-SEM, Carl Zeiss, Supra 40 VP, field emission SEM), and high-resolution transmission electron microscopy (HRTEM) measurements were done using an FEI tecnai G2 Bio-Twin TEM 300 kV. The thermogravimetric analysis (TGA) was carried out using TA instruments. The BET surface area measurements were performed using the Quantachrome-Quadrasorb automatic volumetric instrument. X-ray photoelectron spectra (XPS) were recorded using an Omicron Nanotech XPS of Mg Kα source (1253.6 eV) with CAE analyser mode with a pass energy of 50 eV.

Electrochemical characterisations

The ORR measurements were done using a PARSTAT multichannel potentiostat equipped with a rotator from PINE instruments. A rotating ring-disc electrode (RRDE, PINE Instruments electrode model no. E7R9) with a glassy carbon (GC, diameter 5.6 mm) disk and Pt ring was used as the working electrode (the collection efficiency of the Pt ring is 0.37). The reference and counter electrodes were Ag/AgCl (sat. KCl) and Pt mesh (in a

separate compartment). All the ORR experiments were carried out using an electrochemical cell (170 mL) with O_2-saturated 0.1 M KOH as the electrolyte. The potentials were converted to a reversible hydrogen electrode (RHE) using the equation, E (*vs.* RHE) = $E_{Ag/AgCl}$ + 0.197 + 0.059 pH. Unless mentioned, all the potentials in this manuscript are referred to RHE.

The catalytic ink was prepared as described earlier.[36] 6.88 μL of the ink was drop cast on the GC disk of the RRDE using a micropipette (loading density is 0.4 mg cm^{-2}), and the coating was dried under an N_2 atmosphere. Linear sweep voltammetry (LSV) was done on the disk from 1.1 to 0.2 V at a scan rate of 10 mV s^{-1} for different rotational speeds (400–2500 rpm) in O_2-saturated 0.1 M KOH electrolyte (previously, the background current was measured in N_2-saturated electrolyte). The Pt ring electrode potential was kept at 1.2 V to estimate the H_2O_2 intermediate quantitatively. The OER and HER experiments were performed using a rotating disc electrode (RDE) with 1 M KOH as the electrolyte. The zinc–air battery (ZAB) application was demonstrated using a homemade liquid electrolyte ZAB and solid-state ZAB setup, as described in our previous studies.[37]

Results and discussion

The XRD spectrum of the synthesised pristine $GdCoO_3$ (GCO) is shown in Fig. 2(a). The XRD pattern indicates the peaks positioned at 2θ values confirming the crystalline planes (Table S2, ESI†) corresponding to the $GdCoO_3$ perovskite structure (JCPDS 25-1057)[34] without any impurity peaks corresponding to individual oxides. Also, the XRD patterns of GdO/NC-400, CoO/NC-400, and GCO/NC-400 are depicted in Fig. 2(a). In the case of GdO/NC-400 and CoO/NC-400, the prominent peaks centered at 2θ ∼ 28.6° for GdO/NC-400 and 2θ ∼ 36.3° for CoO/NC-400 correspond to the characteristic peaks of Gd_2O_3 and Co_3O_4, respectively (XRD peaks of individual oxides are given in Fig. S2, ESI†). Meanwhile, the main diffraction peaks of GCO/NC-400 are similar to those of GCO, having diffraction patterns with 2θ values of 23.7 (002), 32.5 (020), 33.1 (112), 34.1 (200), and 48.7° (004). The crystalline size of GCO in the GCO/NC-400 composite was calculated using Scherrer's formula by taking the FWHM of the highly intense diffraction peak indexed to (112). The average grain size of GCO in the GCO/NC-400 composite is calculated to be 44 nm. XRD reveals that the structure of GCO is not affected by changing the weight ratio of GCO, KB, or urea, provided the temperature is maintained at 400 °C during the pyrolysis at N_2 atmosphere (Fig. S3, ESI†). However, some characteristic peaks with diminished intensity and peak position shifts compared with GCO to a lower 2θ value were observed. This shift may be due to defects and distortions in the lattice due to N-doping, suggesting the formation of a GCO/NC composite. The Raman spectra of the composite materials exhibit only carbon peaks, as shown in Fig. 2(b). Two main bands are found in the Raman spectra positioned at 1317 and 1590 cm^{-1}, corresponding to the D and G peaks. The I_D/I_G values of GCO/C-400 and GCO/NC-400 are 1.05 and 1.14, respectively. The incorporation of nitrogen may increase the carbon defects.

The degradation mechanism of the GCO/N-doped carbon composite was studied using TGA (Fig. 2(c) and Fig. S4, ESI†). The TGA profile of pristine GCO indicates that the GCO is thermally stable until 900 °C (Fig. S5b, ESI†). Adding carbon and nitrogen precursors to the GCO shows the weight loss at various temperatures. The GCO + KB mixture shows gradual weight loss until 700 °C. The PXRD after the pyrolysis of the GCO + KB (1 : 2) mixture shows the formation of Gd_2O_3 and Co nanoparticles (Fig. S5c, ESI†). Hence, the weight losses after 450 °C may be attributed to the decomposition of the perovskite structure and small weight losses associated with the oxygen functional group in the carbon substrate. Furthermore, TGA curves of GCO + KB + urea (1 : 2 : 4) show that the perovskite structure is retained until 450 °C, when it decomposes into Gd_2O_3 and Co nanoparticles due to the reduction of $GdCoO_3$ by the addition of urea and carbon, as confirmed by the PXRD taken after TGA analysis (Fig. S5a, ESI†). The TGA profiles of GCO + KB + urea reveal a significant weight loss from 130 to 350 °C owing to urea thermal degradation. The PXRD of the pyrolysed GCO composites indicates the formation of Gd_2O_3 and Co nanoparticles due to the presence of urea and/or KB (Fig. S5d and e, ESI†).

The FE-SEM images of the synthesised materials are shown in Fig. 2(d)–(f). The bare GCO in Fig. 2(d) shows a porous morphology, as reported in the literature. The morphology of KB, GdO/NC-400 and CoO/NC-400 is given in Fig. S6 (ESI†). The SEM images of GCO/C-400 (Fig. 2(e)) show more defined particles than GCO/NC-400 (Fig. 2(f)). The GCO/NC-400 (also GdO/NC-400, and CoO/NC-400) shows a less porous morphology. This may be due to the amorphisation of perovskite due to the addition of urea, which is also evidenced by the decrease in intensity of the PXRD of GCO/NC-400. The SEM-energy dispersive X-ray spectroscopy (EDS) mapping illustrates the consistent distribution of elements throughout the materials (Fig. S7, ESI†). Although the Gd and Co were dispersed throughout the materials, the nitrogen and oxygen were near the carbon. The GCO/NC-400 was further analysed using high-resolution transmission electron microscopy (HR-TEM), as shown in Fig. S8 (ESI†). These images suggest that the perovskite with a size of a few hundred nanometres is embedded into the nitrogen-doped KB matrix. The selected area electron diffraction (SAED) pattern from the perovskite is shown in Fig. S8c (ESI†). The HAADF-STEM image (Fig. S8e and f, ESI†) distinguishes the individual perovskite particles from the carbon support. The electron energy loss spectroscopy (EELS) elemental mapping confirms the presence of Gd, Co, O, C, and N uniformly throughout the sample (Fig. 2(g) and (l)). The positional overlap of Gd and Co EELS mapping indicates the presence of $GdCoO_3$, and the nitrogen is mostly doped into the carbon matrix.

Nitrogen adsorption/desorption analysis was used to examine the pore characteristics of the synthesised compounds, as seen in Fig. S9 (ESI†). The pore size was also analysed using the non-local density functional theory (NLDFT) modelling shown in Fig. S10 (ESI†). The majority of the pores for all the

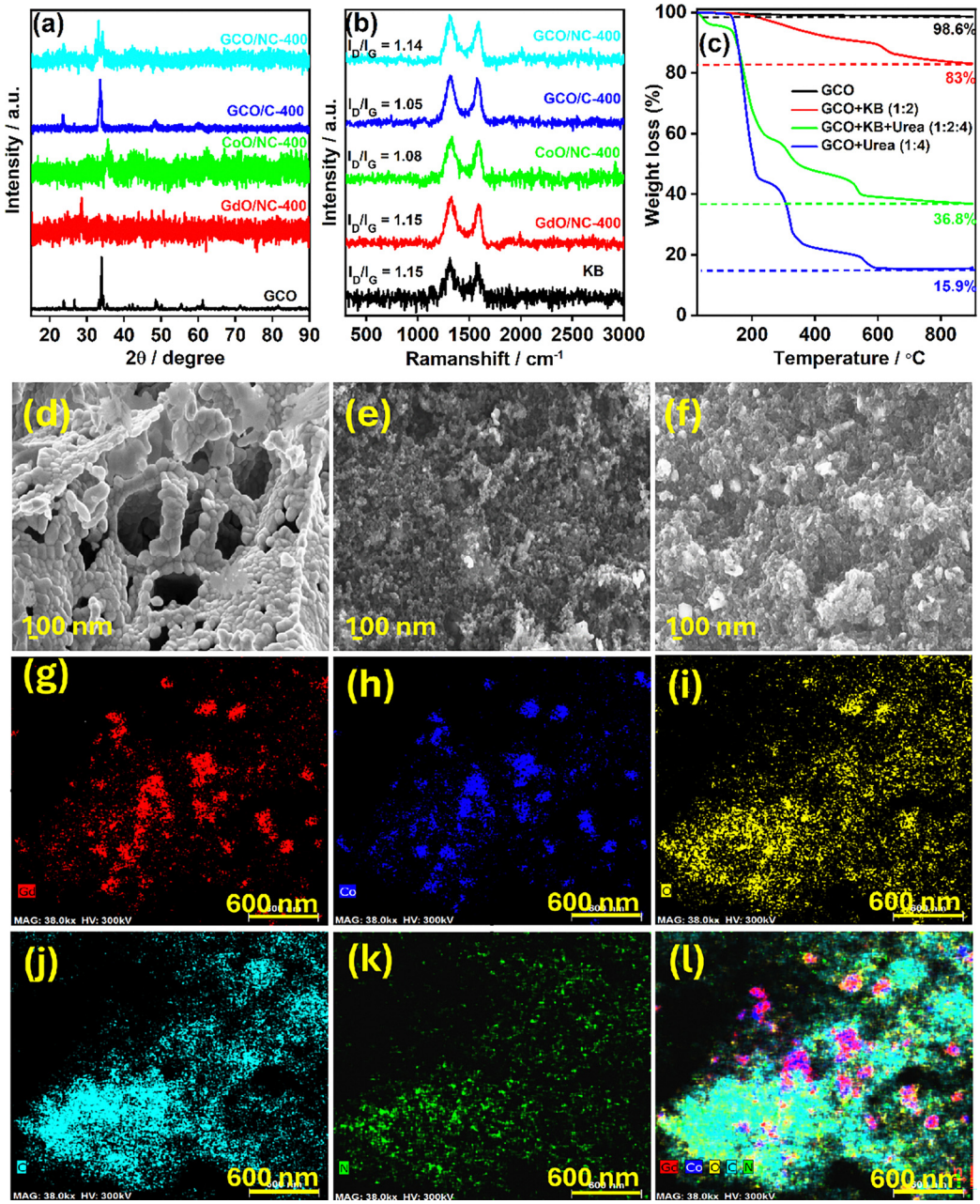

Fig. 2 (a) Powder X-ray diffraction patterns and (b) Raman spectra of the synthesized GCO, GdO and CoO carbon composites, (c) thermogravimetric analysis of GCO, GCO + KB, GCO + KB + urea and GCO + urea in a N_2 atmosphere at a ramp rate of 5 °C min^{-1} from RT to 900 °C, FE-SEM images of (d) GCO, (e) GCO/C-400, and (f) GCO/NC-400, HAADF-STEM EELS elemental mapping of (g) Gd, (h) Co, (i) O, (j) C, (k) N and (l) overlay of all elements present in GCO/NC-400.

composites are found in the mesoporous region. The estimated parameters derived from the BET adsorption isotherms are shown in Table S3 (ESI†). The CoO/NC-400 and GCO/C-400 indicate a type IV BET isotherm with an H3 hysteresis loop, and GdO/NC-400 and GCO/NC-400 exhibit type III isotherms. The BET surface area of GCO/C-400 is 327.6 m^2 g^{-1}, while the surface area drastically decreased to 20.0 m^2 g^{-1} for GCO/NC-400. The reduction in surface area and pore volume may be attributed to the graphitisation of N-doped carbon on top of the porous KB carbon substrate. Furthermore, GCO/NC-400 exhibits a larger pore diameter, which often results in a reduction of surface area.

The elements present in the sample and their corresponding chemical states were studied using X-ray photoelectron spectroscopy (XPS). The XPS survey spectra of GdO/NC-400, CoO/NC-400, and GCO/NC-400 are shown in Fig. S11 (ESI†). The GCO/NC-400 XPS survey spectrum shows characteristic peaks corresponding to the elements of Gd, Co, O, C, and N. Fig. 3(a) shows peaks of Gd-4d$_{5/2}$ and Gd-4d$_{3/2}$ at 142 and 147.9 eV, respectively, revealing the presence of Gd^{3+} in GCO/NC-400.

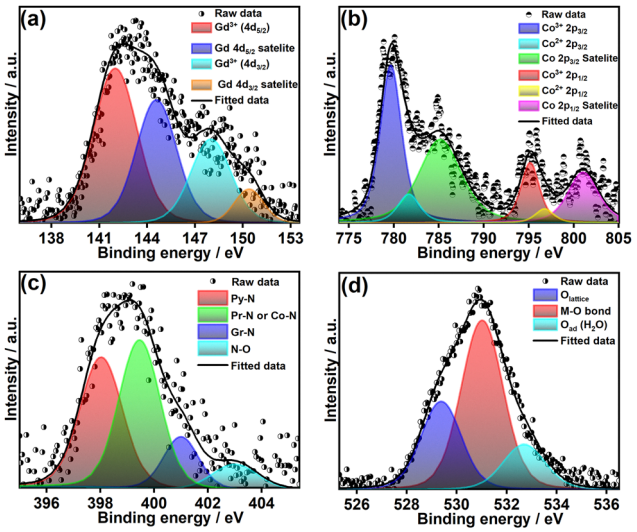

Fig. 3 XPS deconvoluted spectra of core level (a) Gd-4d, (b) Co-2p, (c) N-1s, and (d) O-1s of GCO/NC-400.

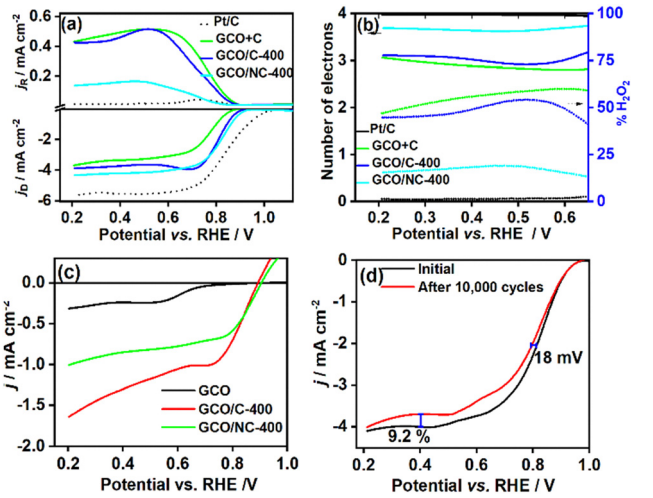

Fig. 4 (a) Hydrodynamic LSV of the ORR on $GdCoO_3$–carbon composites in 0.1 M KOH at a rotational speed of 1600 rpm and 10 mV s^{-1} as the scan rate; (b) potential-dependent number of electrons and % H_2O_2; (c) RDE LSV of H_2O_2 reduction reaction in N_2-saturated 0.1 M KOH electrolyte (contains 2 mM H_2O_2) on GCO/NC-400. The rotational speed is 1600 rpm, and the scan rate is 10 mV s^{-1}. (d) Hydrodynamic voltammogram of ORR on GCO/NC-400 before and after the 10 000 cycles of accelerated durability test.

The deconvoluted Co-$2p_{3/2}$ and Co-$2p_{1/2}$ peaks at 779.7 (Co^{3+}-$2p_{3/2}$), 781.7 (Co^{2+}-$2p_{3/2}$), 795.2 (Co^{3+}-$2p_{1/2}$), and 796.8 (Co^{2+}-$2p_{1/2}$) indicate the presence of Co^{3+} and Co^{2+} (Fig. 3(b)). The lowering of the oxidation state of Co from 3+ to 2+ is attributed to the oxygen vacancies. The amount of oxygen vacancies can be estimated from the area of the Co^{2+} peak. The percentage of oxygen vacancies is 18%, estimated from the Co-$2p_{3/2}$ peak.[38]

The core-level N-1s peak was deconvoluted into four typical forms of nitrogen in the N-doped carbon, *i.e.*, pyridinic-N (Py–N, 398 eV), pyrrolic-N (Pr–N, 399.4 eV), graphitic-N (Gr–N, 401 eV) and nitrogen oxides (N–O, 403.1 eV) (Fig. 3(c)). The core-level O-1s peak was used to study the nature of the oxygen in the perovskite structure. The deconvoluted peaks at 529.3, 531, and 532.7 are referred to lattice oxygen, surface M–O bonds, and adsorbed water molecules (Fig. 3(d)). The deconvoluted C-1s spectrum is given in Fig. S12 (ESI†), indicating the presence of carbon in the form of sp^2-C (284.04 eV), sp^3-C (285.15 eV), C–N or C═O (288.2 eV), and O–C═O (291.3 eV). The deconvoluted XPS spectra for GdO/NC-400 and CoO/NC-400 are given in the ESI† (Fig. S13 and S14).

Oxygen reduction reaction

The hydrodynamic voltammetry was performed in 0.1 M KOH solution to evaluate the ORR performance of the catalysts. The highest activity was obtained for the compound GCO/NC-400 with the E_{onset} = 0.93 V and $E_{1/2}$ = 0.82 V, which is comparable with the benchmark Pt/C catalyst (E_{onset} = 1.01 V and $E_{1/2}$ = 0.85 V), as shown in Fig. 4(a). The individual oxides, such as GdO/NC-400 and CoO/NC-400, were examined for their ORR activity. The RRDE voltammograms of GdO/NC-400 (E_{onset} = 0.87 V and $E_{1/2}$ = 0.69 V) and CoO/NC-400 (E_{onset} = 0.90 V and $E_{1/2}$ = 0.79 V) are given in Fig. S15 (ESI†), suggesting lower ORR activities than GCO/NC-400. Fig. 4(b) shows that the number of electrons (n) is estimated to be 3.7 for GCO/NC-400, indicating that the ORR perhaps follows the 4-electron reduction pathway. The number of electrons is also confirmed from the Koutecký–Levich plots, as shown in Fig. S16 (ESI†). It is important to note that the increase in the number of electrons after the nitrogen doping supports the 4-electron pathway of the ORR. The mechanism of the ORR was further analysed using the H_2O_2 reduction reaction (HPRR). The hydrodynamic voltammetry of HPRR using RDE in N_2-saturated 0.1 M KOH with 2 mM H_2O_2 exhibits a much lower current density compared with the ORR current (Fig. 4(c)). This confirms that the ORR predominantly follows the direct 4-electron pathway rather than the 2 + 2-electron peroxide pathway. The ORR activity was optimised to its best conditions to yield the best ORR activity (Fig. S17, ESI†). The ORR stability test on GCO/NC-400 was performed using an accelerated durability test (ADT). The ADT includes scanning the catalyst-coated GC electrode in the ORR ON and OFF regions at a scan rate of 50 mV s^{-1}. After 10 000 cycles of ADT, the RDE voltammogram was analysed to check the activity degradation of the catalysts. It was observed that a negative shift of 18 mV in the $E_{1/2}$ value is observed in the RDE voltammogram (Fig. 4(d)). The comparison of the real activities between the catalysts can be evaluated after ignoring the effects of mass transport. The mass-transport corrected kinetic current density (j_k) normalised to electrochemical surface area (ECSA) and the mass of the catalyst loading (mass-specific) on the electrode surface are summarised in Table 1. The ECSA of the catalysts was estimated from the reported protocols, as shown in Fig. S18 and Table S4 (ESI†).[39] The GCO/NC-400 exhibits a two to six times increase in the area-specific j_k (19.9 μA cm_{ECSA}^{-2}) and a five to eight times increase in the mass-specific j_k (18.4 A g^{-1}). The obtained area-specific and mass-specific j_k values of the benchmark catalysts are also shown for comparison.

Table 1 Area-specific and mass-specific ORR activities of the synthesised materials with the benchmark Pt/C catalyst

Compounds	I_{DL} (mA)	I_D (mA)	ECSA area (cm_{ECSA}^2)	Area-specific j_k ($\mu A\ cm_{ECSA}^{-2}$)	Mass-specific j_k ($A\ g^{-1}$)
Pt/C	1.37	0.38	2.5[a]	207.0	106.2
GdO/NC-400	1.01	0.18	71.5	3.1	2.2
CoO/NC-400	1.00	0.48	82.5	11.7	9.3
GCO + C	0.85	0.24	10.3	10.1	3.4
GCO/C-400	0.95	0.56	18.1	18.9	13.8
GCO/NC-400	1.06	0.67	20.2	19.9	18.4

The I_D value is taken at the potential 0.9 V for Pt/C and 0.8 V *vs.* RHE for other catalysts. I_{DL} represents the limiting current. [a] The electrochemical surface area of platinum, calculated from the HUPD; the amount of the catalyst coated is 99 μg (corresponds to the 0.4 mg cm^{-2} loading density); the amount of Pt/C coated is 4.95 μg_{Pt}, corresponding to 20 $\mu g_{Pt}\ cm^{-2}$ loading density.

Oxygen evolution reaction

The OER activity of all samples was evaluated using RDE measurements in 1 M KOH solution, as shown in Fig. 5(a). The GCO/NC-400 displayed high OER activity with an E_{10} value (at 10 mA cm^{-2}) of 1.56 V, which is only 60 mV anodic to the benchmark RuO_2 (η = 270 mV) catalyst. Notably, GCO/NC-400 demonstrated higher performance (η = 520 mV) than the benchmark RuO_2 (η = 613 mV) at E_{100}. The Tafel slope of GCO/NC-400 is 87 mV dec^{-1}, indicating the faster initial electron transfer. Also, the E_{10} values of GdO/NC-400 and CoO/NC-400 are 1.75 and 1.58 V, respectively (Fig. S19a, ESI†). The Tafel slope of GdO/NC-400 is very high (235 mV dec^{-1}), whereas the CoO/NC-400 shows a value of 94 mV dec^{-1}, suggesting faster kinetics originated from the B-site of the perovskite (Fig. 5(b) and Fig. S19b, ESI†). A substantial positive shift in the E_{10} value was observed due to the incorporation of nitrogen in the GCO/C-400, indicating the role of nitrogen in enhancing the OER activity. An OER stability test was performed using the chronopotentiometric experiment at the current density of 5 mA cm^{-2}. The GCO/NC-400 shows a stable potential profile up to 30 hours (Fig. 5(c)). The RDE voltammograms after the stability test exhibit only a 14 mV positive shift in the E_{10} value, compared with the initial RDE voltammograms (Fig. 5(d)). The optimisation of various parameters and their voltammograms is shown in Fig. S20 (ESI†). The OER activity of the synthesised materials was evaluated using area-specific (ECSA) and mass-specific kinetic current densities similar to the ORR studies. The GCO/NC-400 exhibits higher area-specific (20.9 μA cm_{ECSA}^{-2}) and mass-specific (19.4 A g^{-1}) kinetic current densities (at 1.55 V) than the other synthesised perovskite/NC materials in this work. The area and mass-specific kinetic current densities of benchmark RuO_2 are also compared and shown in Table 2. The turnover frequency (TOF) of each catalyst was calculated from the procedure reported recently by Sadhukhan *et al.*[40] The TOF of the GCO/NC-400 is estimated as 0.8 s^{-1}, which is close to the benchmark RuO_2 catalyst (1.1 s^{-1}). The TOF values of other catalysts are relatively low for the compound without nitrogen, indicating the role of nitrogen species.

Typically, the bifunctional activity of the electrocatalysts in the metal–air battery application was evaluated by the potential difference between the ORR and OER curves, referred to as ΔE ($\Delta E = \Delta E_{10}^{OER} - \Delta E_{1/2}^{OER}$). The GCO/NC-400 shows a minimum ΔE value of 0.74 V, as shown in Fig. 6(a) and (b), which is a promising bifunctional catalyst compared to most of the recently reported perovskite-based ORR and OER catalysts. The $E_{1/2}$(ORR), E_{10}(OER), and ΔE values of all the composites under study are given in Table S5 (ESI†).

Hydrogen evolution reaction

Besides its bifunctional activity, the GCO/NC-400 exhibits hydrogen evolution reaction (HER) activity in an alkaline medium. The HER performance of the catalysts was investigated in N_2-saturated 1 M KOH solution, as shown in Fig. 7(a). The overpotential (η, potential at which the current density of 10 mA cm^{-2}) measured for the HER for the GCO/NC-400 is 241 mV. The individual oxides on N-doped carbon catalysts show larger overpotentials than the GCO/NC-400 (Fig. S21a, ESI†). The benchmark Pt/C catalyst exhibits the η-value of 20 mV.

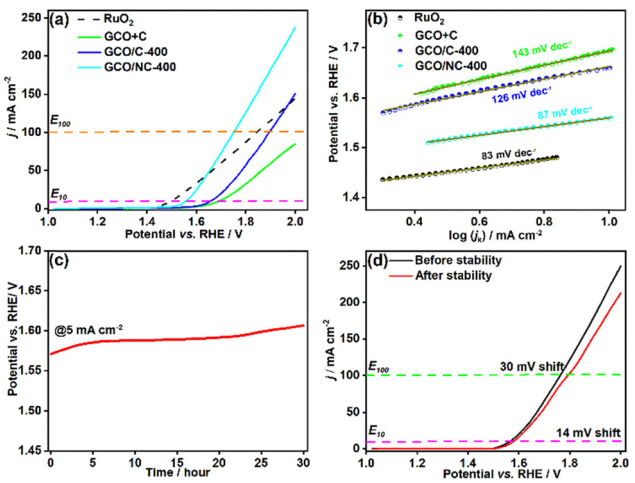

Fig. 5 (a) OER activity of Gd and/or cobalt-based compounds in 1 M KOH as the electrolyte at a scan rate of 10 mV s^{-1} at a rotational speed of 2000 rpm, and (b) the corresponding calculated Tafel slopes using kinetic current. (c) chronopotentiometry stability test of GCO/NC-400 at the current density of 5 mA cm^{-2} and the rotational speed of 2000 rpm. (d) RDE LSV before and after the stability test.

Table 2 Area-specific and mass-specific OER activities of the synthesised materials with the benchmark RuO_2 for comparison

Compound	I_k (mA)	Area-specific j_k ($\mu A\ cm_{ECSA}^{-2}$)	Mass-specific j_k ($A\ g^{-1}$)	Turnover frequency (s^{-1})
RuO_2	5.20	68.5	52.5	1.1
GdO/NC-400	0.43	6.0	4.3	0.2
CoO/NC-400	1.12	13.6	11.3	0.4
GCO + C	0.28	8.5	2.8	0.3
GCO/C-400	0.4	5.5	4.0	0.2
GCO/NC-400	1.92	20.9	19.4	0.8

The I_k values are obtained at 1.55 V; the loading density is the same as that of the ORR, and the loading mass and specific area are similar to Table 1.

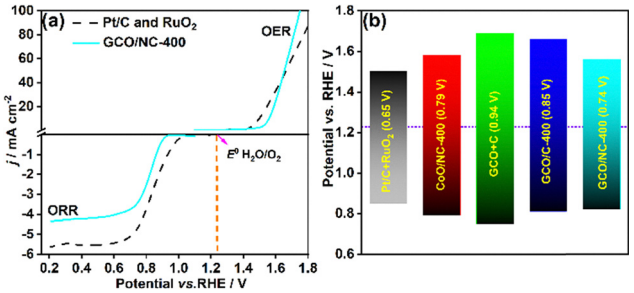

Fig. 6 (a) The ORR and OER activities (bifunctional activity) of the GCO/NC-400 compared with the benchmark catalysts. (b) The bar chart explains the bifunctional activities of all the materials studied in this work.

Table 3 Area-specific and mass-specific HER activities of the synthesised materials with the benchmark Pt/C for comparison

Compound	I_k (mA)	Area-specific j_k (μA cm_{ECSA}^{-2})	Mass-specific j_k (A g^{-1})	Turnover frequency (s^{-1})
Pt/C	9.42	3708.7	1903.0	0.9
GdO/NC-400	0.20	2.8	2.0	0.2
CoO/NC-400	1.52	18.4	15.4	1.0
GCO + C	0.15	4.6	1.5	0.3
GCO/C-400	0.28	3.9	2.8	0.3
GCO/NC-400	2.74	29.9	27.7	2.2

The I_k values are obtained at −0.25 V (other than Pt/C, taken at −0.1 V); the loading density is the same as that of the ORR, and the loading mass and specific area are similar to Table 1.

Interestingly, the GCO/NC-400 shows much lower overpotential compared with the GCO/C-400 (420 mV). The role of N-doping can be realised from the reduction in the significant overpotential values. The kinetics and mechanism of the HER are evaluated through the Tafel analysis. The GCO/NC-400 exhibits a Tafel slope of 143 mV dec^{-1}, suggesting that the mechanism follows the Volmer–Heyrovsky mechanism. There is a sharp contrast in the Tafel slopes (Fig. S21b, ESI†) of GdO/NC-400 (226 mV dec^{-1}) and CoO/NC-400 (243 mV dec^{-1}), larger than GCO/NC-400, indicating their poor HER kinetics as shown in Fig. 7(b). The Tafel slope of GCO/C-400 (138 mV dec^{-1}) is comparable with the GCO/NC-400, indicating the role of the perovskite structure in the kinetics of the HER. The other control sample's HER activity is given in Fig. S22 (ESI†), and a comparison table for HER overpotential is shown in Table S6 (ESI†). The chronoamperometry HER stability test was performed for GCO/NC-400 at the applied potential of −0.24 V for 30 hours. It was observed that the catalyst was very stable, with the retention of 90.9% of the initial current after the electrolysis (Fig. 7(c)). Furthermore, the LSV curve after the stability test shows no change in the overpotential value measured at E_{10} (Fig. 7(d)). Similar to the OER and ORR, the HER activity of the materials is evaluated using the kinetic current densities at a potential close to the E_{10} value (here −0.25 V). The GCO/NC-400 exhibits much higher area-specific activity (29.9 μA cm_{ECSA}^{-2}) and mass-specific activity (27.7 A g^{-1}) compared with other synthesised perovskite/NC materials in this work (Table 3). The TOF was also evaluated and shows the highest TOF (2.2 s^{-1}) among the catalysts studied in this work. A table comparing the ORR, OER and HER activity of GCO/NC-400 with similar reported perovskite materials is given in Table 4.

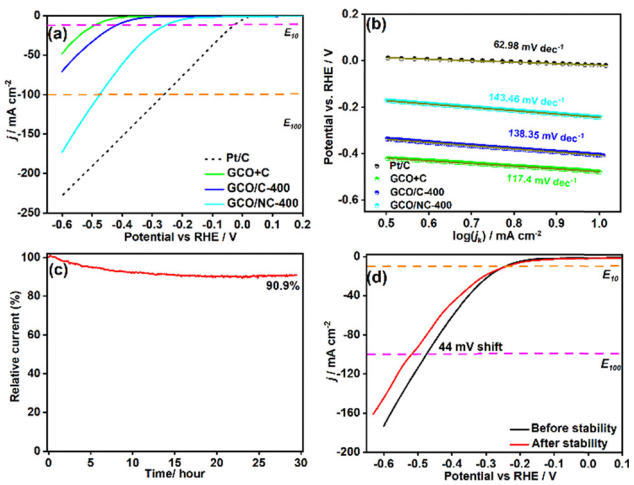

Fig. 7 (a) The LSVs of the synthesized electrocatalysts in the HER region (0 to −0.6 V) in 1 M KOH as the electrolyte and at 10 mV s^{-1} as the scan rate, and 2000 rpm rotational speed, (b) the Tafel plots with slopes, (c) the stability (chronoamperometry) of GCO/NC-400 at a constant potential (−0.24 V, where the current density reaches 10 mA cm^{-2}, and (d) comparison of HER activity before and after the stability test.

Zinc–air battery

A homemade liquid-state rechargeable ZAB was assembled using the GCO/NC-400-coated carbon air electrode, as described in the Methodology section. The GCO/NC-400 coated on the Toray carbon paper exhibits an open circuit potential (OCP) of 1.51 V, which is equal to the commercial Pt/C (1.51 V) catalyst, as shown in Fig. S23a (ESI†). The discharge polarisation curves and the power density plots are shown in Fig. 8(a). The GCO/NC-400 shows a maximum power density of 77 mW cm^{-2} at a current density of 113.6 mA cm^{-2}, which is close to the benchmark Pt/C catalyst (85.0 mW cm^{-2} at a current density of 130.0 mA cm^{-2}). The specific capacity was estimated as 796 mA h g_{Zn}^{-1} for GCO/NC-400, which is close to the theoretical value (820 mA h g_{Zn}^{-1}) (Fig. S23b, ESI†).

Galvanostatic charge–discharge (GCD) cycling studies were performed with a 5 mA cm^{-2} current density for 20 minutes per cycle. Also, the GCD cycles are also tested for the current density of 20 mA cm^{-2} to check the rate capability (Fig. 8(b) and Fig. S24, ESI†). The GCD cycles indicate that the GCO/NC-400 demonstrates higher stability than the commercial Pt/C + Ir/VC, as shown in Fig. 8(c) and Fig. S23c (ESI†). The round-trip efficiency (calculated from the ratio of discharge to charging potential) is estimated as 0.58, wherein the benchmark catalysts (Pt/C + Ir/VC) exhibit 0.60 during the initial cycles. After 200 GCD cycles (66.67 h), the round-trip efficiency of Pt/C + Ir/VC decreased to 0.39, while the GCO/NC-400 shows an efficiency of 0.50. The results indicate that the GCO/NC-400 shows better stability than the benchmark Pt/C+ Ir/VC catalysts.

Table 4 Trifunctionality of some recently reported Gd and/or Co-based perovskites for the ORR, OER and HER catalysts (all the potentials are referred to RHE)

Catalyst	$E_{1/2}^{ORR}$	E_{10}^{OER}	ΔE	E_{10}^{HER}	Ref.
Sr-doped $BaCoO_{3-\delta}$	—	1.6	—	—	41
$LaCoO_3$@rGO	—	1.51	—	—	42
$Sr_{0.95}Nb_{0.1}Co_{0.9-x}Ni_xO_{3-\delta}$	0.75	1.5	0.75	−0.3	43
$(PrBa_{0.5}Sr_{0.5})_{0.95}Co_{1.5}Fe_{0.5}O_{5+\delta}$ & 3D porous N-Gr	—	1.52	—	−0.23	44
$La_{1-x}K_xCoO_3$	—	1.56	—	—	45
CoS_x modified $Pa_{0.5}Ba_{0.5}Mn_{0.25}Fe_{0.75}O_{3-\delta}$	0.69	1.56	0.87	—	46
Cu-doped $GdFeO_3$	—	1.59	—	—	47
$Sm_{0.5}Sr_{0.5}Co_{0.2}Fe_{0.8}O_{3-\delta}$/N-MWCNT	0.68	1.76	1.07	—	48
$Ba_{0.5}Sr_{0.5}Co_{0.8}Fe_{0.2}O_{3-\delta}$	0.64	1.60	0.96	—	49
2 wt% PtO_x + NiO/$GdFeO_3$	0.4	1.42	1.02	—	50
$GdCoO_3$-gC_3N_4	—	1.44	—	−0.23	51
$GdCoO_3$ nanorods	—	1.55	—	—	52
$GdMnO_3$	—	—	—	—	53
$Gd_{0.95}FeO_3$	—	1.64	—	—	54
GCO/NC-400	0.82	1.56	0.74	−0.24	This work

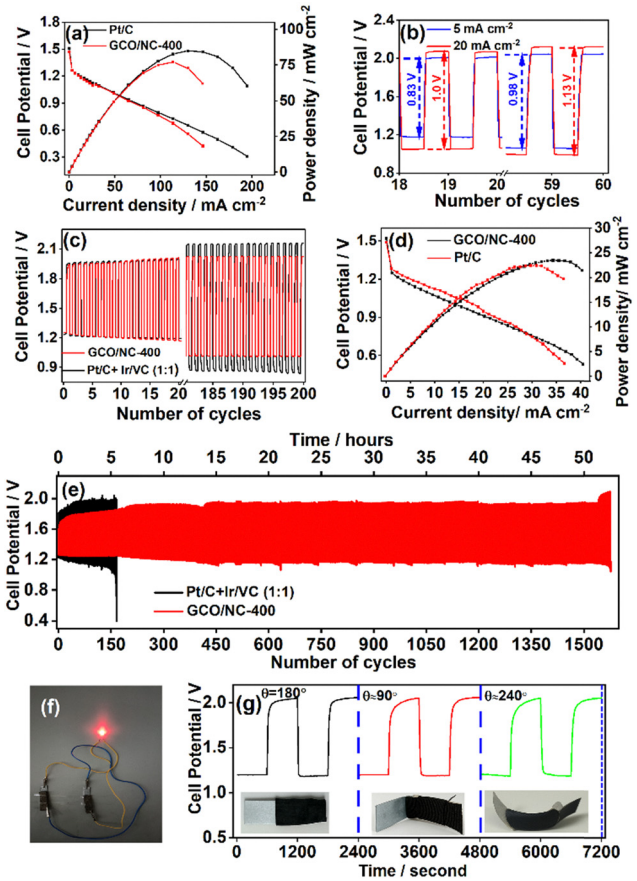

Fig. 8 (a) Polarization and power density plot of GCO/NC-400 and Pt/C using multi-step chronopotentiometry curves, (b) variation of the GCD cycles at different current densities (10 minutes discharging and 10 minutes charging) of GCO/NC-400, (c) GCD cycles of GCO/NC-400 and Pt/C + Ir/VC (1 : 1) for 200 cycles at the current density of 5 mA cm^{-2}, (d) polarisation and power density curves of the solid-state ZAB, (e) GCD cycles of solid-state ZAB coated with GCO/NC-400 catalyst with benchmark (Pt/C + Ir/VC) for comparison, (f) image of the solid-state ZAB powering a red LED and (g) the flexibility of the solid-state ZAB in different angles and their charge–discharge profiles.

A solid-state ZAB using a gel electrolyte was demonstrated with the GCO/NC-400-coated carbon electrode. The GCO/NC-400 exhibits an open circuit potential (OCP) of 1.52 V, as shown in Fig. S25 (ESI†). The discharge polarisation curves of GCO/NC-400 demonstrate a power density of 23.5 mW cm^{-2} at a current density of 34.5 mA cm^{-2}, surpassing that of Pt/C, which exhibits a power density of 22.4 mW cm^{-2} at a current density of 31.1 mA cm^{-2}, as seen in Fig. 8(d). Additionally, the stability of GCO/NC-400 was evaluated using GCD cycles (Fig. 8(e)). The solid-state ZAB of GCO/NC-400 exhibited stable charging and discharging for over 50 hours with good round-trip efficiency. The cycling stability of the Pt/C + Ir/VC-based solid-state zinc–air battery is 5.53 hours. Fig. 8(f) shows the image of a solid-state ZAB device powering a red LED. To study the flexibility of the ZAB device, the charging and discharging experiment was performed at different bending angles of the device, as shown in Fig. 8(g). It was observed that the ZAB charging–discharging profile (and the potentials) did not vary, indicating the flexibility for practical applications. A comparison table of the similar liquid/solid-state ZAB performance is given in Table S10 (ESI†).

The post-mortem characterisation of the GCO/NC-400 composite was performed using powder XRD, Raman spectroscopy, SEM, and EDS (Fig. S26, ESI†). The post-cycling powder XRD pattern shows distinct peaks corresponding to $GdCoO_3$, indicating that $GdCoO_3$ is stable during the charge–discharge process. A number of additional peaks are also obtained in the XRD pattern, referring to ZnO, KOH, K_2CO_3, and potassium acetate. Raman spectra exhibit an increase in intensity ratio (I_D/I_G) from 1.14 (before) to 1.25 (after cycling), signifying an increase in defect density within the N-doped carbon support. The increasing defects can be rationalised by the carbon corrosion, which occurs at the positive potentials. The SEM images reveal a noticeable transformation of surface morphology, with coarsened structures and the appearance of crystalline aggregates, presumably ZnO and salt deposits. These morphological changes indicate surface passivation and partial catalyst degradation.

A comprehensive XPS study was done after 1500 GCD cycles to assess the chemical stability and surface composition changes in the GCO/NC-400 catalyst (Fig. S27 and S28, ESI†). Although the peaks are very noisy to deconvolute, the Co^{2+} and Co^{3+} ratio is calculated as ~18%, and it is more or less close to the value of the initial oxygen vacancy. Although the overall content is not accurate from the XPS measurements, the relative contents of the Co^{2+} and Co^{3+} are unchanged, indicating that the oxygen vacancies remain the same. The N-1s XPS spectrum indicates that the relative weight percentage of typical nitrogen species like Py–N, Pr–N and Gr–N is decreased, while a substantial increase in the N–O is observed, attributed to the oxidation of the nitrogen species during the GCD cycles.

Conclusions

Recent research focuses on developing new materials to improve multi-functional electrocatalysts for electrochemical energy storage and conversion devices. Perovskite-based metal oxides are promising materials due to their tunable electronic properties with A and B-site substitutions. The $GdCoO_3$ on the N-doped carbon material was synthesised using mechano-chemical ball-milling followed by pyrolysis. The synthesised materials show electrochemical oxygen reduction and evolution activities (j_k(ORR) = 18.4 A g^{-1} at 0.8 V; j_k(OER) = 19.4 A g^{-1} at 1.55 V). The bifunctional activity is evaluated from the ΔE (0.74 V), indicating the excellent bifunctionality of $GdCoO_3$-containing N-doped carbon compared to many other perovskites reported in the literature. Besides, it shows excellent HER activity in an alkaline medium with an overpotential of 0.24 V. The ZAB application (liquid electrolyte and gel-electrolyte) was demonstrated with a comparable power density to benchmark Pt/C catalysts.

Conflicts of interest

There are no conflicts to declare.

Data availability

The data supporting this article have been included as part of the ESI.†

Acknowledgements

The authors thank the IISER Thiruvananthapuram for funding and facilities.

Notes and references

1 Y. Meng, W. Song, H. Huang, Z. Ren, S.-Y. Chen and S. L. Suib, *J. Am. Chem. Soc.*, 2014, **136**, 11452–11464.
2 H. Cheng, M.-L. Li, C.-Y. Su, N. Li and Z.-Q. Liu, *Adv. Funct. Mater.*, 2017, **27**, 1701833.
3 J. Li, D. Chu, H. Dong, D. R. Baker and R. Jiang, *J. Am. Chem. Soc.*, 2020, **142**, 50–54.
4 Y. Sun, T. Zhang, P. Sun, J. Wang, W. Duan, Y. Zhuang, L. Wang and Z. Li, *J. Energy Chem.*, 2024, **94**, 778–788.
5 J. S. Sanchez, Z. Xia, K. Mirehbar, S. Sasidharan, S. A. Aravindh, A. Liscio, J. Sun, M. Christian, J. Palma, V. Palermo and R. Marcilla, *J. Mater. Chem. A*, 2024, **12**, 11945–11959.
6 J. Yin, Y. Li, F. Lv, M. Lu, K. Sun, W. Wang, L. Wang, F. Cheng, Y. Li, P. Xi and S. Guo, *Adv. Mater.*, 2017, **29**, 1704681.
7 Y. Fan, S. Ida, A. Staykov, T. Akbay, H. Hagiwara, J. Matsuda, K. Kaneko and T. Ishihara, *Small*, 2017, **13**, 1700099.
8 G. Fu, Z. Cui, Y. Chen, L. Xu, Y. Tang and J. B. Goodenough, *Nano Energy*, 2017, **39**, 77–85.
9 V. Kiran, K. Srinivasu and S. Sampath, *Phys. Chem. Chem. Phys.*, 2013, **15**, 8744–8751.
10 Q. Qin, J. Hao and W. Zheng, *ACS Appl. Mater. Interfaces*, 2018, **10**, 17827–17834.
11 S. Gupta, W. Kellogg, H. Xu, X. Liu, J. Cho and G. Wu, *Chem. – Asian J.*, 2016, **11**, 10–21.
12 C. E. Beall, E. Fabbri and T. J. Schmidt, *ACS Catal.*, 2021, **11**, 3094–3114.
13 J. Suntivich, H. A. Gasteiger, N. Yabuuchi, H. Nakanishi, J. B. Goodenough and Y. Shao-Horn, *Nat. Chem.*, 2011, **3**, 546–550.
14 Y. Zhu, W. Zhou and Z. Shao, *Small*, 2017, **13**, 1603793.
15 X. Xu, W. Wang, W. Zhou and Z. Shao, *Small Methods*, 2018, **2**, 1800071.
16 Y. Wei, Z. Weng, L. Guo, L. An, J. Yin, S. Sun, P. Da, R. Wang, P. Xi and C.-H. Yan, *Small Methods*, 2021, **5**, 2100012.
17 C. Sun, J. A. Alonso and J. Bian, *Adv. Energy Mater.*, 2021, **11**, 2000459.
18 H. Zhu, P. Zhang and S. Dai, *ACS Catal.*, 2015, **5**, 6370–6385.
19 X. Sun, Y. Yuan, S. Liu, H. Zhao, S. Yao, Y. Sun, M. Zhang, Y. Liu and Z. Lin, *Adv. Funct. Mater.*, 2025, **35**, 2416705.
20 A. Grimaud, O. Diaz-Morales, B. Han, W. T. Hong, Y.-L. Lee, L. Giordano, K. A. Stoerzinger, M. T. M. Koper and Y. Shao-Horn, *Nat. Chem.*, 2017, **9**, 457–465.
21 S. Ingavale, M. Gopalakrishnan, C. M. Enoch, C. Pornrungroj, M. Rittiruam, S. Praserthdam, A. Somwangthanaroj, K. Nootong, R. Pornprasertsuk and S. Kheawhom, *Small*, 2024, **20**, 2308443.
22 P. Anand, M.-S. Wong and Y.-P. Fu, *J. Energy Storage*, 2024, **77**, 109917.
23 H. Yu, N. Liedienov, I. Zatovsky, D. Butenko, I. Fesych, W. Xu, C. Song, Q. Li, B. Liu, A. Pashchenko and G. Levchenko, *ACS Appl. Mater. Interfaces*, 2024, **16**, 3605–3620.
24 J. Suntivich, K. J. May, H. A. Gasteiger, J. B. Goodenough and Y. Shao-Horn, *Science*, 2011, **334**, 1383–1385.
25 A. Grimaud, K. J. May, C. E. Carlton, Y.-L. Lee, M. Risch, W. T. Hong, J. Zhou and Y. Shao-Horn, *Nat. Commun.*, 2013, **4**, 2439.
26 E. Fabbri, R. Mohamed, P. Levecque, O. Conrad, R. Kötz and T. J. Schmidt, *ACS Catal.*, 2014, **4**, 1061–1070.

27 Z. Shao and S. M. Haile, *Nature*, 2004, **431**, 170–173.
28 J.-I. Jung, H. Y. Jeong, J.-S. Lee, M. G. Kim and J. Cho, *Angew. Chem., Int. Ed.*, 2014, **53**, 4582–4586.
29 C. Balamurugan, S. Song, H. Jo and J. Seo, *ACS Appl. Mater. Interfaces*, 2021, **13**, 2788–2798.
30 R. R. Mahalik, S. Soren, I. Hota, A. K. Debnath, K. P. Muthe and P. Parhi, *J. Rare Earths*, 2024, **42**, 2078–2087.
31 Z. M. Almarhoon, I. Manzoor, J. H. Shah, H. G. Ozcan, A. G. Abid and S. I. Allakhverdiev, *J. Phys. Chem. Solids*, 2024, **193**, 112217.
32 E. Nandhakumar, P. Selvakumar, A. Sasikumar, M. Prem kumar, E. Vivek and R. Kamatchi, *Mater. Lett.*, 2022, **315**, 132002.
33 E. Omari and M. Omari, *Int. J. Hydrogen Energy*, 2019, **44**, 28769–28779.
34 Y. Liu, W. Zhu, W. Zhang, Z. An, J. Liu and L. Liu, *Inorg. Chem.*, 2023, **62**, 19366–19374.
35 K. Elumeeva, J. Masa, J. Sierau, F. Tietz, M. Muhler and W. Schuhmann, *Electrochim. Acta*, 2016, **208**, 25–32.
36 J. Anjana, A. N. Eledath and A. Muthukrishnan, *Mater. Adv.*, 2023, **4**, 4216–4225.
37 A. N. Eledath, A. Edathiparambil Poulose and A. Muthukrishnan, *ACS Appl. Energy Mater.*, 2024, **7**, 2378–2391.
38 J. Wang, D. N. Mueller and E. J. Crumlin, *J. Eur. Ceram. Soc.*, 2024, **44**, 116709.
39 S. Baskaran, G. P. Mageswari and A. Muthukrishnan, *ChemCatChem*, 2025, e00598.
40 A. Sadhukhan, A. Karmakar, K. Koner, S. Karak, R. K. Sharma, A. Roy, P. Sen, K. K. Dey, V. Mahalingam, B. Pathak, S. Kundu and R. Banerjee, *Adv. Mater.*, 2024, **36**, 2310938.
41 R. Mondal, H. Ratnawat, S. Mukherjee, A. Gupta and P. Singh, *Energy Fuels*, 2022, **36**, 3219–3228.
42 J. Ahmed, T. Ahamad, N. Alhokbany, M. A. Majeed Khan, P. Arunachalam, M. S. Amer, R. M. Alotaibi and S. M. Alshehri, *J. Ind. Eng. Chem.*, 2023, **121**, 100–106.
43 Q. A. Islam, R. Majee and S. Bhattacharyya, *J. Mater. Chem. A*, 2019, **7**, 19453–19464.
44 Y. Bu, H. Jang, O. Gwon, S. H. Kim, S. H. Joo, G. Nam, S. Kim, Y. Qin, Q. Zhong, S. K. Kwak, J. Cho and G. Kim, *J. Mater. Chem. A*, 2019, **7**, 2048–2054.
45 R. Mondal, N. K. Mishra, M. Singh, A. Gupta and P. Singh, *Phys. Chem. Chem. Phys.*, 2022, **24**, 28584–28598.
46 X. Shi, Y. Deng, L. Zhao, Y. Gong, R. Wang, H. Wang and B. He, *Electrochim. Acta*, 2021, **391**, 138951.
47 E. Omari and M. Omari, *Int. J. Hydrogen Energy*, 2019, **44**, 28769–28779.
48 X. Liu, L. Fan, Y. Wang, W. Zhang, H. Ai, Z. Wang, D. Zhang, H. Jia and C. Wang, *Int. J. Hydrogen Energy*, 2023, **48**, 15555–15565.
49 X. Wu, H. Miao, R. Hu, B. Chen, M. Yin, H. Zhang, L. Xia, C. Zhang and J. Yuan, *Appl. Surf. Sci.*, 2021, **536**, 147806.
50 C. Balamurugan, S. Song, H. Jo and J. Seo, *ACS Appl. Mater. Interfaces*, 2021, **13**, 2788–2798.
51 Z. M. Almarhoon, I. Manzoor, J. H. Shah, H. G. Ozcan, A. G. Abid and S. I. Allakhverdiev, *J. Phys. Chem. Solids*, 2024, **193**, 112217.
52 E. Nandhakumar, P. Selvakumar, A. Sasikumar, M. Prem kumar, E. Vivek and R. Kamatchi, *Mater. Lett.*, 2022, **315**, 132002.
53 R. R. Mahalik, S. Soren, I. Hota, A. K. Debnath, K. P. Muthe and P. Parhi, *J. Rare Earths*, 2024, **42**, 2078–2087.
54 E. Omari and M. Omari, *Ceram. Int.*, 2024, **50**, 25509–25517.